CHALMERS
UNIVERSITY OF TECHNOLOGY

Temporal survey of P- A nd L-band polarimetric backscatter in boreal forests

Citation for the original published paper (version of record):
Monteith, A., Ulander, L. (2018). Temporal survey of P- A nd L-band polarimetric backscatter in boreal forests. IEEE Journal of Selected Topics in Applied Earth Observations and Remote Sensing, 11(10): 3564-3577. http://dx.doi.org/10.1109/JSTARS.2018.2814825

Temporal Survey of P- and L-Band Polarimetric Backscatter in Boreal Forests

Albert R. Monteith, *Student Member, IEEE*, and Lars M. H. Ulander, *Fellow, IEEE*

***Abstract*—Environmental conditions and seasonal variations affect the backscattered radar signal from a forest. This potentially causes errors in a biomass retrieval scheme using data from the synthetic aperture radar (SAR) data. A better understanding of these effects and the electromagnetic scattering mechanisms in forests is required to improve biomass estimation algorithms for current and upcoming P- and L-band SAR missions. In this paper, temporal changes in HH-, VV-, and HV-polarized P- and L-band radar backscatter and temporal coherence from a boreal forest site are analyzed in relation to environmental parameters. The radar data were collected from a stand of mature Norway spruce (*Picea abies* (L.) Karst.) with an above-ground biomass of approximately 250 tons/ha at intervals of 5 min from January to August 2017 using the BorealScat tower-based scatterometer. It was observed that subzero temperatures during the winters cause large variations (4 to 10 dB) in P- and L-band backscatter, for which the HH/VV backscatter ratio offered some mitigation. High wind speeds were also seen to cause deviations in the average backscatter at P-band due to decreased double-bounce scattering. Severe temporal decorrelation was observed at L-band over timescales of days or more, whereas the P-band temporal coherence remained high ($>$0.9) for at least a month neglecting windy periods. Temporal coherence at P-band was highest during night times when wind speeds are low.**

***Index Terms*—Backscatter, boreal forest, L-band, P-band, synthetic aperture radar (SAR), temporal coherence, time series.**

I. Introduction

FOREST variables such as above-ground biomass and tree height can be estimated from synthetic aperture radar (SAR) data. This is of interest for generating maps of these parameters for forest management and for monitoring forests degradation and deforestation [1]. Most importantly, forest biomass estimates will allow for improved data of the global terrestrial carbon flux which is the largest uncertainty in our current understanding of the carbon cycle [2]. Filling this knowledge gap will allow for improved climate change predictions and provide scientific support for international treaties and agreements [3], [4].

Two frequency bands that have been allocated to SAR remote sensing and are of high interest for forest biomass estimation are P-band (centered at 435 MHz) and L-band (centered at 1270 MHz). This interest is mainly due to their ability to penetrate the canopy and scatter off the stems and larger branches, which contain the majority of the biomass. This opportunity for biomass estimation using a P-band SAR will be exploited by ESA's BIOMASS mission, which is scheduled for launch in 2021 [3]. BIOMASS will feature a fully polarimetric P-band SAR and the orbits will allow repeat-pass SAR interferometry and tomography. An L-band SAR, namely JAXA's ALOS-2, is already in orbit and features repeat-pass SAR interferometry [5]. Repeat-pass SAR interferometry and tomography at L-band and higher frequencies are less suitable for forest remote sensing due to high temporal decorrelation, introducing a need for a single-pass SAR interferometer at L-band. DLR's Tandem-L mission is planned to fill this need [6].

In addition to above-ground biomass, electromagnetic waves at P- and L-bands are also sensitive to changes in the geometry and dielectric properties of the forest and ground which vary due to environmental and seasonal changes. Such variations can cause both an offset and temporal variation in the forest backscatter [7]–[11]. The P-band backscatter for the copolarized channels (HH and VV) is believed to be dominated by the double-bounce scattering mechanism in boreal forests, which is sensitive to soil, stem and branch moisture, and terrain undulation [12]–[14]. L-band electromagnetic waves are more scattered and attenuated by the forest canopy, making them less affected by the double-bounce mechanism. Compared to the ground and tree trunks, the geometry of the forest canopy is less stable in time due to time-varying forces exerted by wind and precipitation. This results in higher temporal decorrelation at L-band compared to P-band, whereas lower frequencies (VHF-band) are even less affected by environmental effects while featuring improved sensitivity to higher biomass ranges [15]–[17]. However, VHF-band SAR is less suitable for spaceborne implementation due to the impact of the ionosphere [18].

Temporal decorrelation is of special concern in repeat-pass SAR interferometry and tomography, where several successive acquisitions are required for reconstructing an interferogram or tomographic profile. If changes in forest geometry and moisture between acquisitions are large then this temporal decorrelation cannot be separated from decorrelation due to the sensor geometry, affecting the quality of parameter estimates using SAR

Manuscript received October 31, 2017; revised February 7, 2018; accepted February 28, 2018. Date of publication April 10, 2018; date of current version October 15, 2018. This work was supported by the Hildur and Sven Wingquist Foundation for Forest Research, the European Space Agency, and the Swedish National Space Board. *(Corresponding author: Albert Monteith.)*

A. R. Monteith is with the Department of Space, Earth and Environment, Chalmers University of Technology, Gothenburg SE-412 96, Sweden (e-mail: albert.monteith@chalmers.se).

L. M. H. Ulander is with the Department of Space, Earth and Environment, Chalmers University of Technology, Gothenburg SE-412 96, Sweden, and also with the Radar Systems Unit, Swedish Defence Research Agency (FOI), Linkping SE-581 11, Sweden (e-mail: lars.ulander@chalmers.se).

Color versions of one or more of the figures in this paper are available online at http://ieeexplore.ieee.org.

Digital Object Identifier 10.1109/JSTARS.2018.2814825

interferometry and tomography observables [19], [20]. For the BIOMASS mission, up to seven acquisitions, each separated by three days, are needed for tomographic reconstruction [3]. This requires high coherence over such timescales at P-band. At L-band, coherence over timescales in the order of a second is necessary for single-pass SAR interferometric acquisitions since repeat-pass interferometry is not suitable at such high wavelengths.

Attempts have been made to mitigate the effects of temporal variation of SAR observables in biomass estimation models using polarimetric and multitemporal SAR image combinations. Yet the electromagnetic scattering mechanisms in forests and how they are affected by environmental and seasonal variations are still poorly understood for L- and P-bands SAR. This knowledge gap must be filled to improve forest parameter estimation algorithms. Tower-based stations measuring the polarimetric tomographic radar response from tropical forests over long timescales have been set up in French Guiana and Ghana [21], [22]. The radar instrument in these experiments acquired measurements in the frequency range of 400 MHz to 1 GHz at 15 min intervals. A similar study on a single temperate tree has revealed that very different seasonal changes occur in the P-band backscatter and coherence at higher latitudes, especially during frozen periods [15]. However, these results cannot be extrapolated to boreal forests due to significant differences in forest geometry and climate [23]. Boreal forests are characterized by conifers, which have mostly vertical trunks and relatively small branches. The branches represent a small fraction of the total tree volume, which is dominated by the vertical trunk, accentuating the double-bounce mechanism. Compared to tropical forests, boreal forests are also subjected to subzero temperatures. The seasonal variation of environmental parameters is particularly strong in the boreal zone which is primarily due to the high latitudinal variation of solar insolation at these high latitudes [24]. These differences motivate further investigations in the temporal variation of radar backscatter in boreal forests.

The tower-based campaign, BorealScat, was initiated in 2016 to study the variation in scattered electromagnetic fields in a forest site representative of boreal forests [25]. The BorealScat radar system operates at P-, L-, and C-band (centered at 5400 MHz) and is capable of fully polarimetric tomographic radar acquisitions [26]. The 50-m high tower (see Fig. 1) is equipped with two antenna arrays: one for P- and L-band consisting of 20 antennas and one for C-band consisting of 10 antennas. An on-site weather station provides data that allow investigations into how the radar signatures are affected by weather parameters over timescales from less than a second to years.

The aim of this paper is to help answer the following questions.

1) What effects do the environmental parameters have on the measured backscatter and temporal coherence at P- and L-band at HH, VV, and HV polarization?
2) In what conditions and at what time intervals is the backscatter most stable and temporal coherence highest?
3) What polarimetric combinations mitigate unwanted changes in the backscatter?

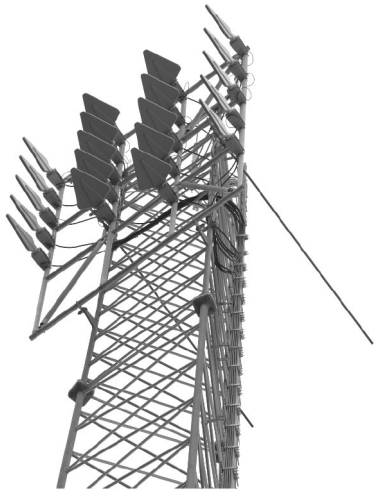

Fig. 1. Photo of the antenna array including the 20 log-periodic antennas. The outer two columns are vertically polarized and the inner two columns are horizontally polarized.

In this study, data from January to August 2017 using four of the P/L-band antennas from BorealScat were analyzed. Section II will provide some background on the ecophysiology and electrical properties of trees. In Section III, the experimental setup, forest site, and data collection method are described. Section IV details the processing methods used in this analysis, Section V discusses the temporal stability of the radar system, and Section VI covers the experimental results and analysis. The paper is concluded in Section VII with a summary of the main results.

II. Background

The radar backscatter of forests is sensitive to the dielectric properties of living vegetation, which is dominated by its temperature and moisture content at a given frequency [27]. The rate of soil moisture uptake and transpiration vary with environmental conditions and with ecophysiological control systems within the trees, resulting in a dynamic wood moisture content.

The driving force of transpiration is the vapour pressure deficit (VPD), which is the difference between the partial pressures of water vapor in the air and in the leaf/needle tissue. In this paper, VPD will be normalized to standard atmospheric conditions at sea level (101.325 kPa) to give the units of Pa/kPa, such that 1 Pa/kPA is equal to 1 mbar/bar. A VPD in the range of 8 to 12 Pa/kPa results in healthy transpiration, conducting water in the trees xylem vessel from the soil to the leaves, where it evaporates as water vapor, maintaining an equilibrium [28]. Under a high VPD ($>$16 Pa/kPa), more water in the stem and branches is lost due to transpiration than can be replaced by water uptake in the soil, resulting in a net decrease of stem moisture and dielectric constant. However, conifers can limit water loss by closing their stomata.

During winter periods in boreal forests the VPD is low ($<$4 Pa/kPa), resulting in little transpiration. Instead, a dynamic complex dielectric constant of wood arises from freeze-thaw cycles. At temperatures above 0 °C, the dielectric constant of

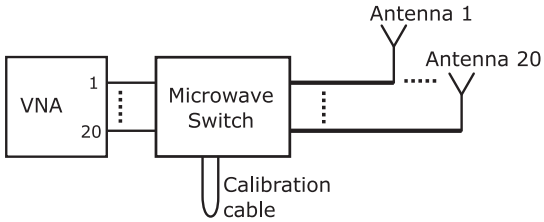

Fig. 2. Block diagram of the radar system. The thick lines are 60-m low loss cables leading up the tower. Both the VNA and switch are interfaced with a controlling computer automating measurements.

TABLE I
RADAR SYSTEM PARAMETERS

Band	Centre frequency, f_c [MHz]	Bandwidth, B [MHz]	Frequency step, δ_f [MHz]	Half-power antenna beamwidth
P	435	30	0.5	E-plane: 68° H-plane: 114°
L	1307.5	135	0.5	E-plane: 60° H-plane: 98°

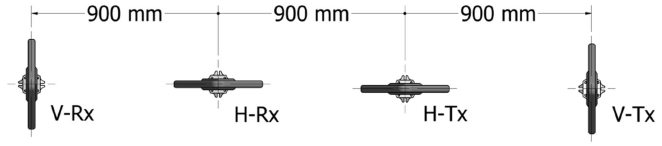

Fig. 3. Antenna geometry (to scale) used in this experiment, as viewed from the front of the array. The outer antennas are vertically polarized, while the inner two antennas are horizontally polarized. The right two antennas transmit, while the left two receive the scattered field.

Fig. 4. Photo from inside the forest under observation (left), dominated by vertical trunks, and the canopy (right) consisting of randomly orientated branches and needles.

spruce wood remains mostly constant for a given water content [27]. As the air temperature drops below 0 °C, water within trees remain in a metastable, supercooled liquid state [29]. Under certain conditions, ice nucleation occurs and ice propagates through the tree at a rates of 2 to 4 mm/s [30]. The time and location of this ice nucleation is inherently random, but is most likely to occur at the bases of branches in the canopy. The latent heat released by this freezing process has been detected in the canopy of Norway spruce (*Picea abies* (L.) Karst.) using thermocouplies and infrared cameras [31]. For liquid water, the real part of the dielectric constant is approximately 80, whereas for ice, it is close to 3 [32], causing a large, rapid drop in backscatter as temperatures drop below 0 °C. This effect has been observed at L-band [11], [33]–[37], and at P-band [13].

III. EXPERIMENT DESCRIPTION

A. Experiment Hardware

The radar system consists of a vector network analyser (VNA), a mechanical microwave switching network, 20 parallel 60-m long low-loss coaxial cables connected to an array of 20 antennas at the top of the tower as shown in Fig. 2. The 20-port VNA (Rohde&Schwarz model ZNBT8) generates the signal transmitted by the antennas and receives the signals corresponding to the scattered field captured by the antennas.

The microwave switch serves the purpose of connecting any two of the ten transmit and ten receive VNA ports across a calibration cable for performing an internal calibration. During measurements, each of the 20 VNA ports is connected to one of the 20 antennas (Rohde&Schwarz model HL040E) at the top of the tower via the microwave switch and a 60-m low loss cable. These linearly polarized log-periodic antennas have a maximum gain of 6 dBi and half-power beamwidths as detailed in Table I. Their weather-resistant radomes allows for more reliable measurements in varying environmental conditions. The 20-element antenna array was designed to allow fully polarimetric tomographic imaging, but for this experiment, only the results from the upper four antennas are used. Two antennas transmit (H and V polarization), while two of the antennas receive (H and V polarization) as shown in Fig. 3. These four antennas are at the top of the array at a height of approximately 50 m above the ground and horizontally separated by 0.9 m to minimize mutual coupling. The boresight of each antenna points horizontally in the same direction.

Weather parameters are also measured at the site. Air temperature, relative humidity, and air pressure are measured at the ground level as well as at 35 m above the ground. A heated tipping rain gauge provides precipitation measurements, but cannot distinguish between rain and snow. Snow depth observations measured daily at 6:00 at a weather station 2.5 km to the east were therefore also included in this study. Two 3-D ultrasonic anemometers at the top of the tower provide accurate measurements of the wind speed and direction during all weather conditions. Soil moisture sensors within the forest stand provide measurements of the volumetric water content (VWC).

Measurements are fully automated by an onsite server and data are transferred to Chalmers University of Technology twice a day via 4G.

B. Site Description

The forest stand under observation in this experiment lies within the Remningstorp experimental forest site in southern Sweden. The stand is dominated by mature *P. abies* with little undergrowth due to thinning. The ground topography is mostly flat (see Fig. 4) and height of trees vary from 25 m close to the tower to 27 m further away. In the fall of 2014, this forest stand had an estimated above-ground biomass of approximately 250 tons/ha. All trees within a 10-m diameter plot within the stand with a diameter at breast height greater than 4 cm were calipered and the heights of 25% of the trees were measured. Above-ground biomass was estimated using allometric

equations [38], and extended to the plot level using airborne lidar scans trained and validated on multiple plots in Remningstorp.

C. Data Collection

The VNA generates a stepped-frequency continuous-wave signal with the parameters shown in Table I. A frequency step of $\delta_f = 0.5$ MHz gives an unambiguous range of 300 m. The intermediate-frequency bandwidth of the VNA was set to 10 kHz, resulting in a minimum dynamic range of 100 dB. During a measurement sequence, the frequency sweep is transmitted by ten antennas, one at a time, while simultaneously receiving the scattered field with all 20 antennas every time. Such a measurement sequence is repeated every 5 min. The data collected by the VNA are S-parameters, which give both the magnitude and phase of the received fields relative to the transmitted field at each frequency. For each antenna, the frequency sweep was repeated four times over a time interval on the order of 200 ms. Coherent averaging (averaging the real and imaginary part of the received signal) of the four sweeps was done to increase the signal-to-noise ratio and decrease the amount of data stored while preserving the phase. It was later observed that wind events cause severe decorrelation at L-band in high winds but less at P-band, after which the four sweeps were instead stored individually for later processing. The data are therefore divided into two data sets. Data set 1 consists of the coherently averaged sweeps from the time period January 9 to June 9, 2017 and Data set 2 of the individual frequency sweeps from the period June 9 to August 4, 2017. Investigations relating to coherence and spread in the backscatter were only performed using Data set 2 to avoid biases due to decorrelation.

Meteorological parameters from the weather station were averaged every 10 min (integrated in the case of precipitation). After noticing the short-term decorrelation due to wind, the instantaneous air temperature, relative humidity, pressure, wind speed, and wind direction were also stored at the start of each radar measurement sequence since June 9, 2017 to support the analysis of short-term dynamics of radar signatures. Every 30 min, an internal reference measurement was taken through the calibration cable (see Fig. 2) between each transmit–receive VNA port to verify the VNA stability. Some soil moisture data were lost during the winter period due to technical problems.

IV. Processing Methods

A. Range Profiles

A range profile (scattered amplitude versus range) can be computed by taking the inverse discrete Fourier transform (iDFT) of the measured s-parameters. Due to the finite bandwidth, sidelobes will be present in the range profile, which can be reduced by first applying a Hamming window to the S-parameters. The S-parameters are also first corrected for losses and phase shifts in the 60-m low-loss cables as measured in the lab. The complex range profile can be expressed as

$$s_{ij}^k(R) = \text{iDFT}\left\{S_{ij}^k(f) \cdot W(f) \cdot C^{-1}(f)\right\} \tag{1}$$

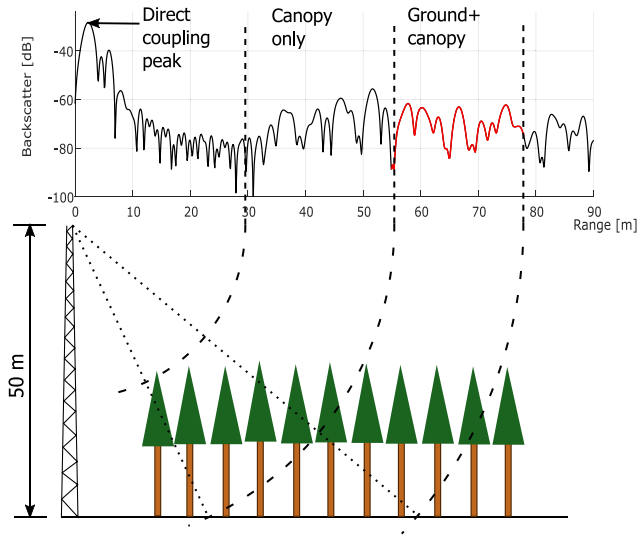

Fig. 5. Diagram of the acquisition geometry and how it relates to a range profile (L-band, HH in this example). This range profile is the magnitude of the complex range profile before compensation for free-space loss, i.e., $|s_{ij}^k(R)|$. The tower is on the left, looking toward the right. Dotted lines extend toward the 25° and 50° incidence angle positions on the ground, defining the backscatter region of interest. The red region in the range profile is the 55 to 78 m region (incidence angle range of 25° to 50° at the ground surface) which is used to estimate the backscatter. This region includes reflections from both the forest and ground.

which is corrected for free-space loss as

$$r_{ij}^k(R) = R^2 \cdot s_{ij}^k(R) \tag{2}$$

where i and j are the indices of the transmitting and receiving antennas, respectively, that determine the polarization combination (HH, VV or HV), k is the time index which is different for each 5-min measurement sequence, R is the slant range, $S_{ij}^k(f)$ are the S-parameters measured by the VNA, $W(f)$ is the Hamming window, and $C(f)$ is the two-way frequency response of the low-loss cable as measured in the lab. The iDFT length is equal to $f_s/\delta_f + 1$, where the implicit sampling rate f_s must be larger or equal to the bandwidth B to satisfy the Nyquist criterion. An oversampling factor of 12 was used to accurately define the range gate. An example of a range profile $s_{ij}^k(R)$ for HH polarization at L-band is shown in Fig. 5, along with the acquisition geometry. In the 0- to 5-m slant range interval of the range profile, a peak originating from direct coupling between the transmitting and receiving antenna appears, followed by reflections off the tower structure. In the 29- to 50-m interval reflections from the forest canopy appear and from 55 m onwards, the response originates from both the canopy and ground reflections.

B. Backscatter

Backscatter was estimated by averaging the reflected power over the 55 to 78 m portion of the range profile in order to reduce speckle variance. This corresponds to the incidence angle range of 25°–50° at ground, and includes responses from both the ground and forest (see Fig. 5). This is the incidence angle range featured by spaceborne SAR systems. The backscatter

estimate can be expressed as

$$\sigma_{ij}^{k} = \frac{ME^{k}}{N\lambda^{2}} \sum_{R=55}^{78} \left| r_{ij}^{k}(R) \right|^{2} \tag{3}$$

where N is the number of range profile samples in the 55 to 78 m region and λ is the wavelength corresponding to the center frequency f_c. E is a compensation factor for variations in cable attenuation, described in the next section. The factor M is an unknown constant dependent on the antenna gain pattern, iDFT normalization, and the transmitted power. This provides a time series of the backscatter with k as the time index and an equidistant sampling interval of 5 min. Note that this is a measure of the relative backscatter and is not calibrated in an absolute sense. This is not a problem because in this experiment only relative changes in backscatter with time are of interest. The factor M was therefore set to 1. For Data set 1, $S_{ij}^{k}(f)$ is the coherent average of the four frequency sweeps, whereas for Data set 2, the term $|r_{ij}^{k}(R)|^{2}$ is averaged over the four frequency sweeps.

The averaged 55 to 78 m portion of the range profile does not offer a high number of independent spatial looks, especially at P-band (4 and 24 independent number of looks at P- and L-bands, respectively). This results in a backscatter estimate with high variance. This variance can be reduced by averaging σ_{ij}^{k} in the time domain using a Hamming-weighted, 3-h long (36 samples) moving-average filter. This will be referred to as the backscatter trend. But this will only improve the backscatter estimate during periods of high variance with time. In periods of low variance, the backscatter estimate may be biased due to constant space-dependent constructive and destructive interference of electromagnetic waves scattered by the forest. However, variations due to environmental changes can still be observed.

C. Compensation for Variations in Cable Attenuation

Significant systematic errors can occur due to changes in the electrical characteristics of the 60-m low loss cables and antennas, which are subjected to the outdoor environment. The direct coupling peak in the range profile (see Fig. 5) offers a measure of the antenna and cable response between the transmit–receive ports, which should be constant with time, assuming that the antenna pattern remains constant with time. The backscatter estimates were therefore corrected by normalizing for changes in the magnitude of the direct coupling peak relative to the median of the peak magnitude. The compensation factor E at time instant k was calculated as

$$E^{k} = \frac{\text{Median peak power}}{\text{Peak power at time } k} \tag{4}$$

i.e., the median of the peak power over all time instants k is divided by the peak power at time instant k. The median is used instead of the mean for better resilience against outliers and a skewed distribution. The peak powers were calculated from $|s_{ij}^{k}(R)|^{2}$, before compensation for a free-space loss, which would suppress this peak.

D. Temporal Coherence

The complex coherence in the received signal relative to a reference time instant with index k was estimated by

$$\gamma_{ij}(\Delta k) = \frac{\sum_{R=55}^{78} r_{ij}^{k}(R) \cdot r_{ij}^{k+\Delta k}(R)^{*}}{\sqrt{\sum_{R=55}^{78} \left| r_{ij}^{k}(R) \right|^{2} \cdot \sum_{R=55}^{78} \left| r_{ij}^{k+\Delta k}(R) \right|^{2}}} \tag{5}$$

where Δk is the time interval in samples between the two observations. This accounts for changes in phase and signal shape with time due to geometric and moisture changes in the forest and ground, which is detrimental to repeat-pass SAR interferometry and tomography at timescales of days. This measure is not affected by changes in average backscatter due to the normalization factor in the denominator. Only the magnitude of the complex coherence, $|\gamma_{ij}(\Delta k)|$, will be analyzed in this paper. This serves as a correlation coefficient of the scattered field between different times.

E. Wavelet Coherence

Wavelet coherence was used to reveal possible links between two time series. Traditionally this is done using measures such as the cross-correlation or the cross-spectral density in Fourier analysis. But these methods assume that the time series are stationary, which is not valid for forest backscatter. Wind events, rainfall, and seasonal changes are expected to affect the mean, variance, and periodicities of the forest backscatter with time, resulting in a nonstationary process. Wavelet coherence can be used to reveal local correlations between two time series at different timescales, making it suitable for a nonstationary time series. A moving correlation between two time series may also reveal local similarities between two time series, but not when a phase shift exists between them. Short-time Fourier transform methods are suitable when short-term correlations with phase shifts exist, but low-frequency behavior is under-represented due to the short time windows [39]. Wavelet coherence is robust to phase shifts between the two series because it provides both a measure of common power (the wavelet coherence magnitude) and the phase shift, similarly to the cross-spectral density. This is useful in this experiment since there is often a delay between a weather event such as a rapid change in temperature and a corresponding change in backscatter. Readers interested in how the wavelet coherence and its 5% confidence intervals are calculated are referred to [40]. The Morlet wavelet was used because it provides a better frequency resolution than other common wavelets [41], which is important to separate diurnal variations from other transients.

V. System Stability

The calibration cable measurement offers a measure of VNA measurement stability with time. The variation in these measurements was less than 0.02 dB which is insignificant compared to the backscatter variations and will therefore not be discussed further.

The direct coupling peak also exhibited variations much smaller than variations in backscatter, but these variations were large enough to motivate their compensation. Fig. 6 shows an

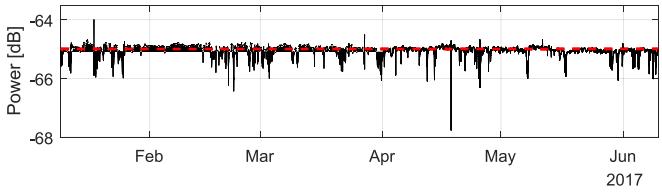

Fig. 6. Plot of the direct coupling peak power between the H-Tx and H-Rx antennas at P-band used for normalizing variations in the cable attenuation. The dashed red line shows the corresponding median for which the backscatter data in the channel are normalized for. The peaks coincide with rainfall events, likely due to a wet radome, and are treated as outliers.

example of the direct coupling peak for HH at P-band. The red line indicates the median, to which the compensation is made. The large peaks coincided with rainfall events, but corresponding changes in the backscatter were not observed. This indicates a change in the antenna pattern due to wet radomes. These peaks were therefore treated as outliers and were not included in the correction factor E^k used in estimating the backscatter. Outliers were defined as values more than three local standard deviations from the local mean over a window length of 8000 samples.

VI. Results

A. Seasonal Variations

Boreal forests are found at high latitudes, subjecting them to highly dynamic weather conditions throughout the year. Data set 1 allows the investigation of seasonal changes in backscatter because it starts during the winter and ends in the summer. The backscatter for HH, VV, and HV for P- and L-bands, along with the corresponding trends and environmental parameters from January to June 2017, are shown in Fig. 7. During winter conditions (up to mid-March), the backscatter seems to vary in phase with temperature, especially during subzero conditions, causing deviations of 4 to 10 dB in the backscatter. The decrease in backscatter during subzero temperatures is most likely dominated by a freezing ground. But the decrease in backscatter is just as strong for HV-polarized backscatter as for the copolarized backscatter, even though this component is believed to be not as sensitive to the double-bounce mechanism. The drop in the backscatter is also significant at L-band, which is expected to be attenuated by the canopy in this dense forest, decreasing the contribution of the ground. These observations suggest that the freeze-thaw cycle of the soil is not the only mechanism at play causing these large variations in the backscatter during the winter. These large rapid variations in the backscatter are also believed to be due to increases in the ice fraction of the stems. The copolarized backscatter at P-band shows similar patterns with temperature throughout the winter period. This observation agrees with a previous study on a lodgepole pine (*Pinus contorta* L.) stand, where it was shown that the liquid water content of the stems showed large variations in phase with temperature during the winter [42]. This varying ice fraction in the stems would result in a varying dielectric constant of the stems and a change in backscatter. The presence of snow on the ground (5 to 8 March) does not appear to have a large influence on the backscatter at P- and L-bands. A rise in the soil moisture is seen when this snow melts, but the corresponding increase in the backscatter may just be due to the air temperature rising from subzero to above-zero as seen during the rest of the winter season.

During the spring period (mid-March to beginning of May), the backscatter still shows large variations, but on the time scale of days. This is because the temperature tends to drop below 0 °C at night, leaving the ground partially frozen during the day. During the day, the VPD reaches values of 5 to 10 Pa/kPa, which are suitable for transpiration, but the frozen soil does not allow the trees to replace the moisture lost to the atmosphere. This variation in tree water content, and thus the backscatter, can be seen in all polarizations at both P- and L-bands, indicating that the water content varies throughout the entire vertical extent of the trees.

In summers (beginning in May), the backscatter is more stable because there is little freezing of the ground and in the stem, and the liquid water in the soil can replace what is lost to transpiration, maintaining the equilibrium. The largest variations in this period coincide with rainfall events and strong winds. For the copolarized channels at both P- and L-bands, this period seems to show a long-term decrease in average backscatter of 1 to 2 dB compared to the spring period. This could be due to the decrease in soil moisture content and higher rates of transpiration due to the increased temperature and VPD in May, resulting in a net decrease of the stem water content. Such a change in the stem water content during this period was also observed in [42].

The diurnal variations appeared to coincide more with near diurnal wind speed cycles than VPD. Large variations are seen in all backscatter trends whenever the wind speed exceeds 5 m/s. This was quickly realized to be largely due to the coherent averaging of the four frequency sweeps which results in a decrease in the backscatter when wind causes temporal decorrelation on the subsecond timescale. This data set should therefore not be used for investigating diurnal cycles, the effects of wind or temporal coherence.

This seasonal transition in backscatter variance is clearly seen in the magnitude-squared wavelet coherence between backscatter and air temperature shown in Fig. 8. A strong coherence is seen between backscatter and air temperature during the winter period at timescales longer than a day for both bands and all polarizations. These variations are clearly separated from diurnal variations, which intermittently occur with time. During the growing season (after mid-March), the diurnal variations in the backscatter are broken by rainfall events which cause transients in the measured backscatter. The σ_{ij}^k backscatter series were used to generate the wavelet coherence plots. If the backscatter trend is used instead, the plots look the same except for lower coherence at time scales less than half a day.

B. Polarimetric Relationships

The backscatter from polarization channels HH, VV, and HV exhibit different relationships with one another for above-zero and subzero temperatures. This is shown in Fig. 9 where scatterplots relate the backscatter for the polarization channels at P- and L-bands, separated by above- and subzero temperatures. Only

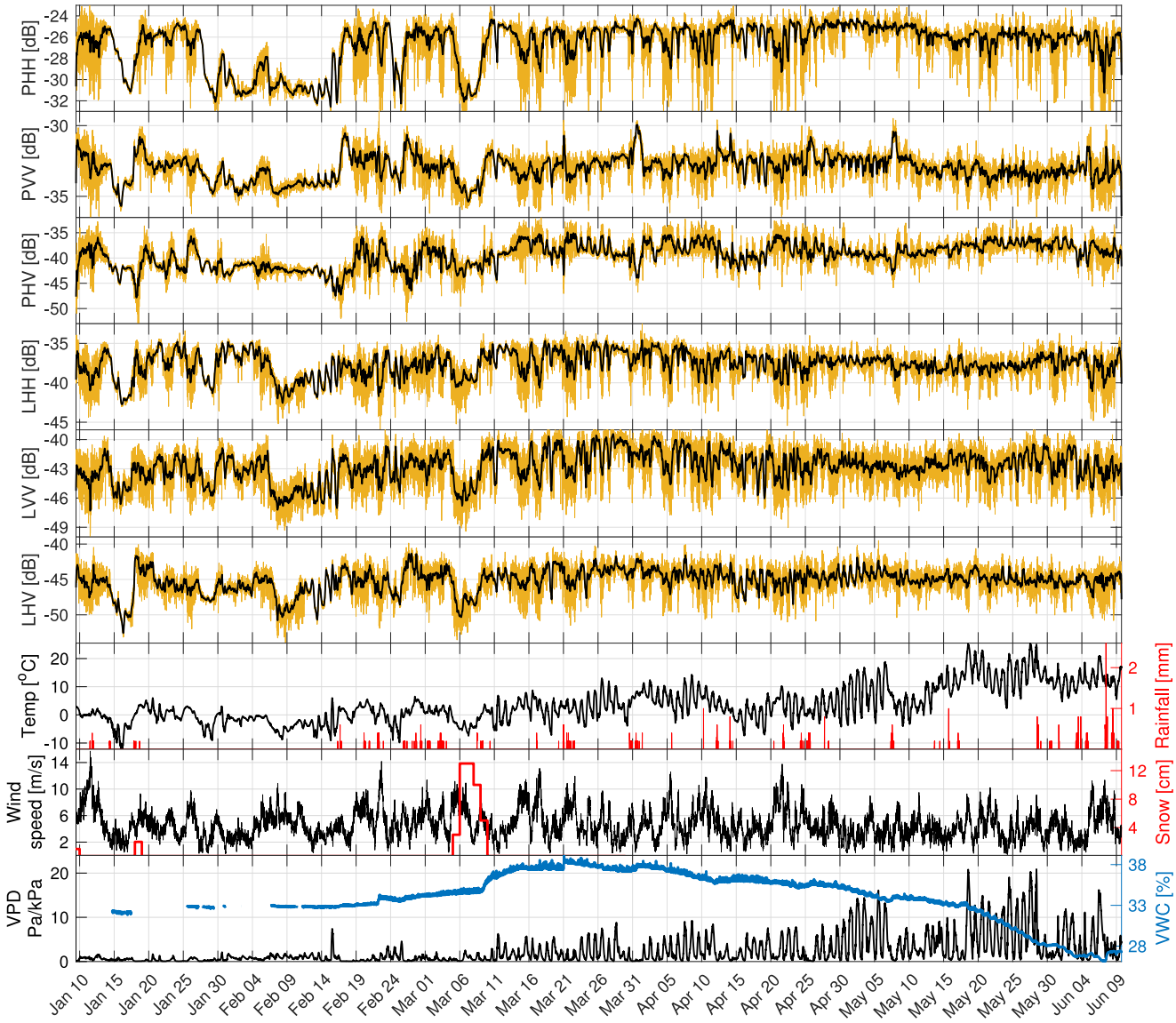

Fig. 7. Time series of P- and L-band relative backscatter and environmental parameters. PHH = P-band HH polarization, PVV = P-band VV polarization, PHV = P-band HV polarization, and LHH = L-band HH polarization. The orange curves are the backscatter measurements, σ_{ij}^{k}, and the darker curves in the backscatter plots show the corresponding trends. The dashed line in the plot of air temperature shows the 0 °C temperature line to easily distinguish between above- and subzero temperatures. The snow time series is the daily snow depth observations. The soil moisture content is given in units of VWC. The backscatter measurements tend to vary slowly but over large ranges during the winter and then stabilize during the summer.

data from times when the wind speed was less than 5 m/s were used to avoid backscatter biases due to incoherent averaging of decorrelated frequency sweeps. The strongest relationship is between HH and VV for both P- and L-bands at subzero temperatures, where a linear regression fit gives a coefficient of determination of 0.67 in both cases. This agrees with the linear relationship that has been observed between temperature and the dielectric constant of spruce wood for a fixed moisture content [27].

From the strong linear relationship between HH and VV, one would expect decreased sensitivity to environmental variables for the HH/VV trend. The median absolute deviation (MAD) will be used to measure this spread in the backscatter since the distributions are skewed. The MAD values for HH, VV, and HH/VV backscatter trends at P-band were 0.57, 0.53, and 0.39 dB at P-band when including backscatter data during both above- and subzero temperatures but for wind speeds lower than 4 m/s. This decrease in the spread for the HH/VV ratio agrees with results in [8]. For L-band, the MAD values for HH, VV, and HH/VV backscatter trends are 0.93, 0.93, and 0.63 dB, respectively. This motivates the inclusion of the HH/VV ratio in biomass estimates, especially since it has shown sensitivity to biomass [8].

C. *Effect of Wind on Backscatter*

To avoid the error in the backscatter caused by coherent averaging during windy conditions, the four individual frequency sweeps gathered every 5 min were stored from July 9, 2017 onwards. This allows the computation of the incoherent

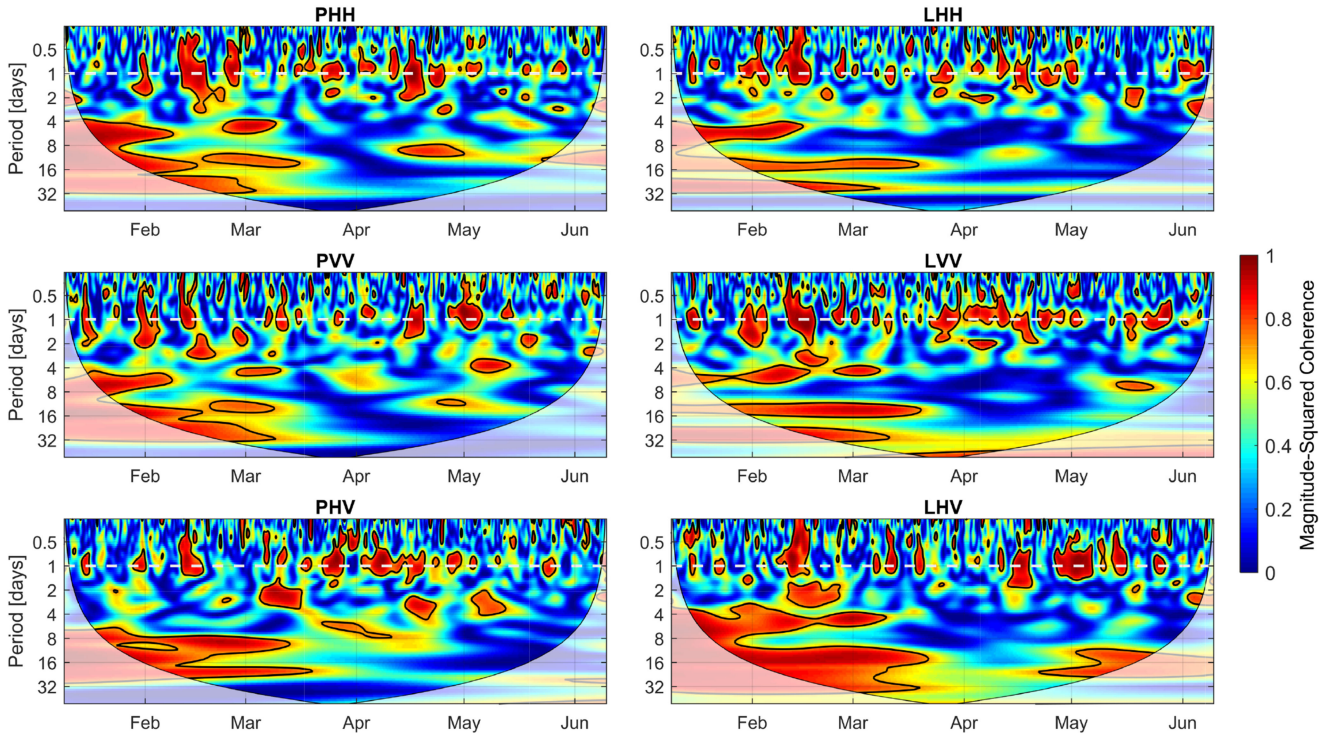

Fig. 8. Squared magnitude of the wavelet coherence between relative backscatter and air temperature during the January to June period in 2017. The black contours indicate the 5% significance level and the dashed white line indicates the 1-day period line. High coherence along this line indicates diurnal cycles. The shaded white regions lie outside the cone of influence where edge effects reduce the certainty of coherence estimates [39]. A strong relationship is seen between the backscatter and temperature during the winter months, which is lost during the growing season (after mid-March), except for short periods with subzero temperatures.

average, which when averaged in time is not susceptible to short-term (subsecond) decorrelation due to wind. Backscatter time series comparing the coherent and incoherent averaging results are shown in Fig. 10. A difference between the black and red curves is a measure of decorrelation on the time scale of 1 s. As expected, the coherently averaged backscatter is lower than the incoherently averaged backscatter during windy conditions, especially at L-band, explaining the drops in the backscatter seen in Fig. 7 during high wind events. This reveals that there is significant temporal decorrelation at L-band even at the subsecond time scale. For VV polarization, the L-band backscatter shows constant short-term decorrelation, even during low wind speed conditions. The same behavior was independently observed for other VV channels in the BorealScat data, ruling out the possibility of a systematic error. This observation could not be explained with the available data.

The drops in backscatter seen in Fig. 7 are avoided if consecutive frequency sweeps are averaged incoherently, but only for L-band. At P-band, the backscatter bias due to short-term decorrelation (difference between the black and red curves) is small ($\leq$1 dB), but a change in the backscatter is seen during windy conditions even for incoherently averaged frequency sweeps, indicating that the drop previously seen in backscatter was not only due to short-term decorrelation. For the copolarized channels at P-band, the backscatter seems to drop with high winds whereas for the cross-polarized channel, the backscatter seems to increase with high winds.

To get a better understanding of what is happening during high and low wind events, the relevant portions of the range profiles for HH-polarized backscatter are shown in Fig. 11 for the times T_1 to T_4 as indicated in Fig. 10. This region is the same as the Ground + canopy region shown in Fig. 5. During windy conditions (times T_1 and T_3), the range profiles show changes between times T_1 and T_3 as well as short-term decorrelation during these times at both P- and L-bands. This is expected since wind causes a change in geometry causing a change in the phase and shape of the range profile. During quiet conditions (times T_2 and T_4), the range profiles are different for L-band, which is likely due to increased sensitivity to geometrical changes over the 6-day interval from T_2 to T_4 because of the shorter wavelength. But for P-band, the range profiles during quiet conditions look almost exactly the same, indicating that for P-band there exists a stable, maximum-backscatter geometrical configuration of the forest present only in low-wind conditions. This stable configuration in this conifer forest consists of vertical stems, which becomes distorted when the wind blows, causing trees to bend. Trees bent over a flat ground exhibit similar monostatic scattering behavior to vertical stems on a sloped ground due to the double-bounce mechanism, for which the backscatter has been shown to reduce significantly ($\sim$10 dB) even for small changes ($\sim 2^\circ$) in the ground slope [12]. This is analogous to varying the angle of a dihedral corner reflector off 90°, which decreases the radar cross-section and explains the observed drop in the copolarized backscatter at P-band during windy conditions. The increase in

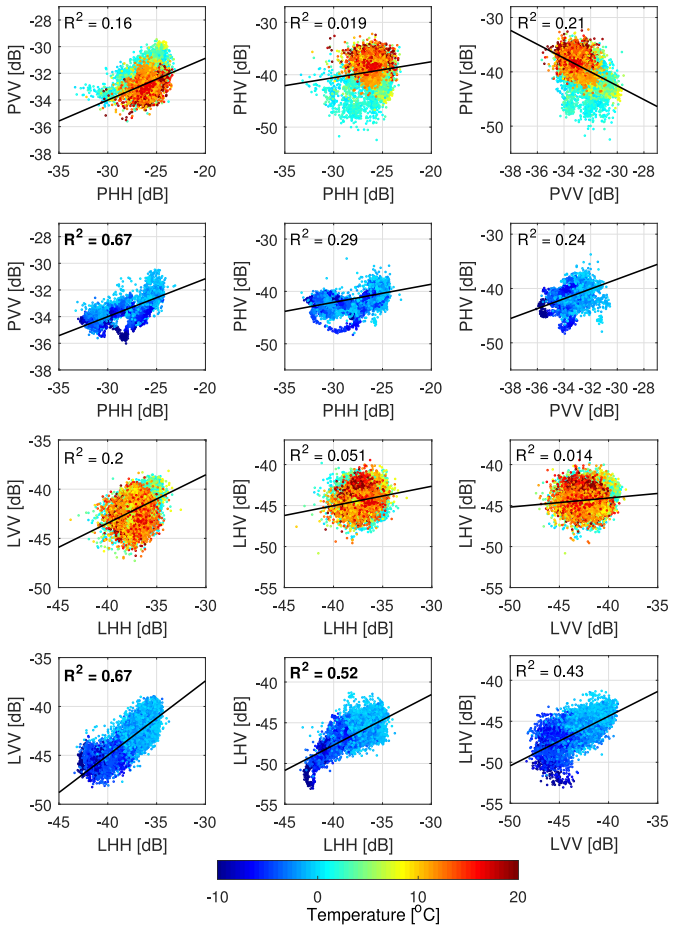

Fig. 9. Scatter plots relating relative backscatter polarization channels. Black lines show the least-squares lines. The coefficient of determination R^2 is indicated in the upper-left corner and is in boldface if larger than 0.5. The first and third rows use data for air temperatures above 0 °C, whereas the second and fourth rows use data from subzero temperatures. This separation shows that there is a stronger linear relationship between the different channels at subzero temperatures, especially between the HH and VV channels, compared to above-zero temperatures.

the HV backscatter during windy conditions can be explained by the depolarization caused by trees bent over a flat ground.

At L-band, attenuation by the canopy and increased sensitivity to ground roughness and stem bending due to the shorter wavelength decreases the double-bounce scattering. Therefore, the mean copolarized backscatter is not significantly affected by wind. The cross-polarized backscatter at L-band does however show an increase with high winds, which is most likely due to the depolarization caused by tilted tree tops.

D. Summer Period

The complete incoherently averaged backscatter time series for HH, VV, and HV for P- and L-bands are shown in Fig. 12, along with environmental parameters. Since wind speed exhibits a diurnal variation during dry conditions, so does the backscatter at P-band. If these diurnal variations were due to transpiration, one would expect to see a negative correlation between the VPD and backscatter. While such a negative correlation is observed, it cannot be separated from the drops in the backscatter due

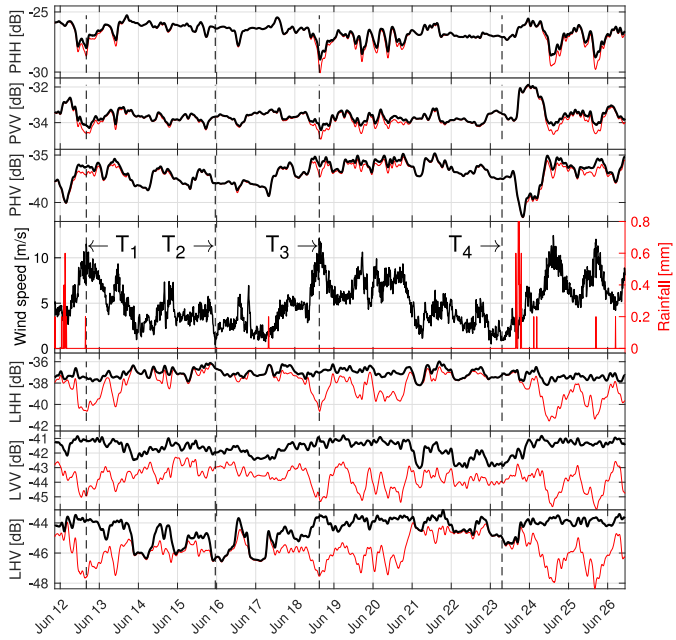

Fig. 10. Comparison of relative backscatter time series trends from coherently and incoherently averaged measurements. The thick lines show the backscatter from incoherent averaging and the thin red lines show the backscatter from coherent averaging. Differences between the lines indicate short-term decorrelation. T_1 to T_4 indicate times for which the range profiles are shown in Fig. 11. The wind speed is the instantaneous wind speed at the time of radar measurements. Changes in the P-band backscatter are still seen for incoherently averaged measurements (black lines), which are due to the trees bending over a flat ground, reducing the double-bounce scattering.

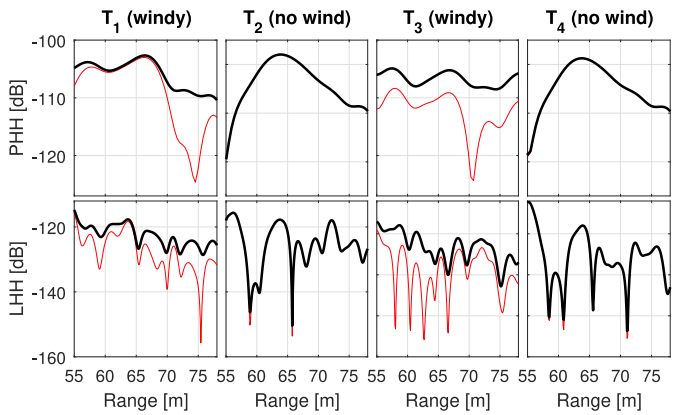

Fig. 11. Range profile sections at the times T_1 to T_4 as indicated in Fig. 10. The thick lines show the relative backscatter from incoherent averaging and the thin red lines show the relative backscatter from coherent averaging. P-band backscatter shows a stable configuration (due to straight stems) during quiet conditions, but L-band does not. Similar results are seen for PVV and PHV.

to wind. This is because since both wind speed and VPD have common power at the diurnal scale (see Fig. 13). Wavelet analysis revealed some intermittent diurnal variations in the L-band backscatter at all polarizations, but the time series were too short to reliably explain these dynamics.

Rainfall seems to cause an increase in VV and decrease in HV backscatter at P-band but little change in HH. One clear example of such an event is on June 24, when the wind speed was low. Rainfall appeared to be the strongest influence of L-band

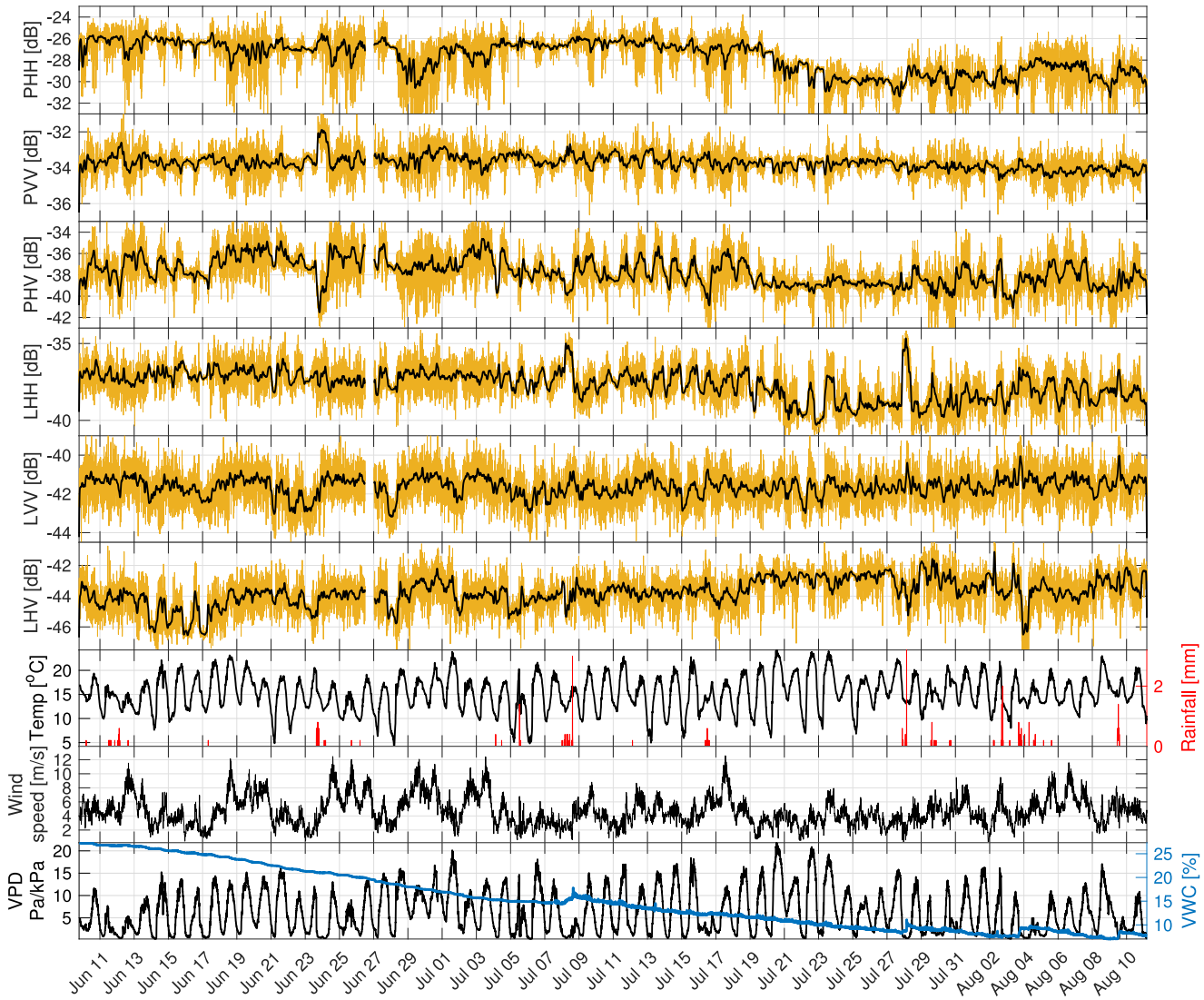

Fig. 12. Time series of P- and L-band relative backscatter and environmental parameters for the summer period. The orange curves are the backscatter measurements, σ_{ij}^{k}, and the darker curves in the backscatter plots show the corresponding trends. The dynamics change toward the end of July, which is believed to be due to a change of seasons (summer–autumn), resulting in a decrease in soil and stem moisture.

backscatter variations, causing large increases in HH backscatter and large decreases in HV backscatter during rainfall (before the rain gauge tips). This indicates sensitivity to canopy wetness at L-band.

At the end of July, the dynamic behavior of the scattered fields changes. A slow decrease in the backscatter is seen in the HH and HV channels at P-band and HH at L-band, with an increase seen in HV at L-band. This can be explained by the high VPD around 21 July during decreasing soil moisture conditions, driving transpiration faster than what can be replaced by water uptake. This trend in the backscatter seems to continue until the rainfall events at the end of July, when the trend begins to reverse, but does not fully recover. The measured decrease in the soil moisture content and hypothesized decrease in the tree moisture content during June and July agree with a previous study on red spruce (*Picea rubens* L.) [43]. A continued series is needed to reveal whether this dynamic behavior continues. The MAD values for HH, VV, and HH/VV backscatter trends at P-band were 0.40, 0.21, and 0.36 dB, respectively, for the summer period up to before the change of season (20 July 2017), showing some decrease in spread compared to HH alone.

E. Backscatter Statistics

Histograms of the P- and L-band backscatter are shown in Fig. 14, separated into the winter period (9 January to 20 March) and the spring/summer growing period (20 March to 11 August). The corresponding mean, median, and standard deviation for each histogram are shown in Tables II and III. For L-band, histograms for only the summer period (9 June to 11 August) are shown to avoid the bias caused by coherent averaging in windy conditions present in Data set 1. During the winter period, the P-band backscatter histograms have bimodal distributions due to freeze-thaw cycles, resulting in large standard deviations. The HH- and HV-polarized backscatter at P-band showed the largest variation during the winter time. During the

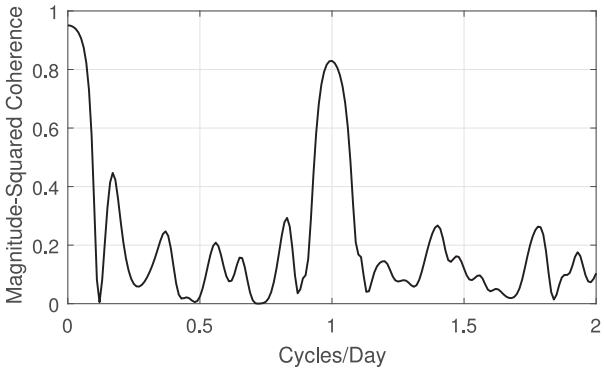

Fig. 13. Magnitude-squared coherence between the wind speed and VPD during the summer period. The peak at 1 Cycles/Day shows that both time series exhibit a strong correlation at the diurnal time scale. This makes it difficult to separate the effects of wind speed and VPD on backscatter if diurnal variations in the backscatter are seen.

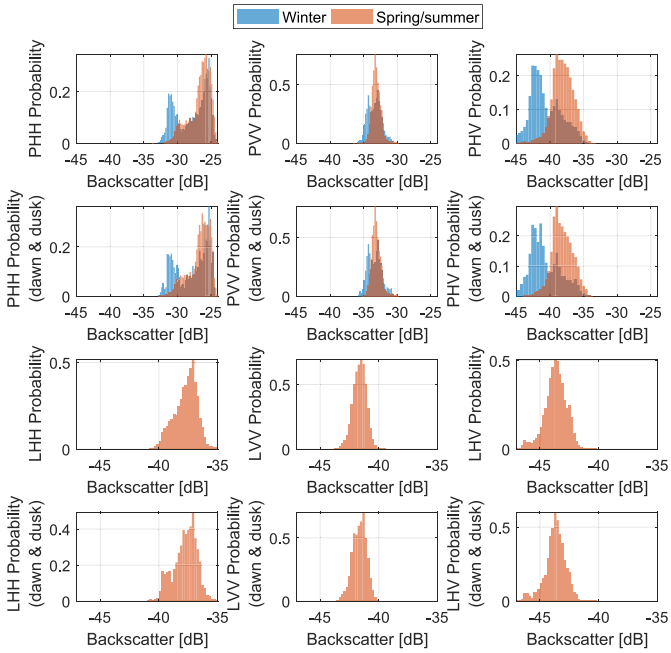

Fig. 14. Histograms of P- and L-band relative backscatter for the winter period and for the spring/summer period. The second and fourth rows include only measurements within the 5:00 to 7:00 and 17:00 to 19:00 periods (dawn/dusk orbit pass times). The bar heights are the number of counts normalized to the sample size and bin width, making the histograms estimates of the probability density function suitable for comparison. During winter the histograms have a bimodal distribution due to freeze-thaw cycles. In summer, the distributions are unimodal, but with more spread in this mode due to moisture content variations.

spring/summer time, the histograms have unimodal distributions. For P-band, the standard deviations during the growing period are lower compared to that of the winter period, but the histograms show that the spread of the predominant mode is larger. This is due to long-term variations due to changes in moisture conditions seen in the time series plots. For both P- and L-band, the HH- and HV-polarized backscatter have larger standard deviations than VV during the growing period.

Fig. 14 and Tables II and III also show the histograms and statistics for the backscatter during only the local times when a SAR satellite in a dawn/dusk sun-synchronous orbit is likely to pass over boreal forests: 6:00 $\pm$ 1 h and 18:00 $\pm$ 1 h. No significant difference in the backscatter statistics was seen for the dawn and dusk periods compared to the complete data set. This motivates the mitigation for environmental effects on backscatter in forest parameter estimation algorithms using backscatter at P- and L-bands.

TABLE II
P-BAND RELATIVE BACKSCATTER STATISTICS FOR THE WINTER PERIOD (9 JANUARY TO 20 MARCH) AND SPRING/SUMMER GROWING PERIOD (20 MARCH TO 11 AUGUST)

Statistics including all times of the day.

Parameter	Mean [dB]	Median [dB]	Std. dev. [dB]
PHH (winter)	-27.8	-27.1	2.4
PHH (spring/summer)	-26.7	-26.3	1.6
PVV (winter)	-33.3	-33.3	1.0
PVV (spring/summer)	-33.1	-33.2	0.7
PHV (winter)	-40.8	-41.3	2.4
PHV (spring/summer)	-38.1	-38.1	1.5

Statistics for only dawn and dusk times.

Parameter	Mean [dB]	Median [dB]	Std. dev. [dB]
PHH (winter)	-27.7	-27.0	2.4
PHH (spring/summer)	-26.7	-26.4	1.6
PVV (winter)	-33.3	-33.3	1.0
PVV (spring/summer)	-33.1	-33.2	0.7
PHV (winter)	-40.9	-41.4	2.4
PHV (spring/summer)	-38.2	-38.3	1.5

The upper table includes data from all times of the day, whereas the lower table only includes data from local dawn (5:00 to 7:00 h) and dusk (17:00 to 19:00 h) times.

TABLE III
L-BAND RELATIVE BACKSCATTER STATISTICS FOR THE SUMMER PERIOD (9 JUNE TO 11 AUGUST)

Statistics including all times of the day

Parameter	Mean [dB]	Median [dB]	Std. dev. [dB]
LHH (summer)	-37.7	-37.6	1.0
LVV (summer)	-41.6	-41.6	0.6
LHV (summer)	-43.7	-43.6	0.9

Statistics for only dawn and dusk times

Parameter	Mean [dB]	Median [dB]	Std. dev. [dB]
LHH (summer)	-37.8	-37.6	1.0
LVV (summer)	-41.7	-41.6	0.6
LHV (summer)	-43.7	-43.7	0.9

The upper table includes data from all times of the day, whereas the lower table only includes data from local dawn (5:00 to 7:00 h) and dusk (17:00 to 19:00 h) times.

F. Temporal Coherence

Other than biasing the backscatter, wind also decreases the temporal coherence at P-band, as can be seen in the temporal coherence plots of Fig. 15. The coherence series in this plot were calculated with respect to a reference time (June 10, 2017, 03:05 h) when the instantaneous wind speed was very low ($\sim$0.5 m/s). During quiet conditions, which is usually at night, the temporal coherence is high ($>$0.95) for the copolarized channels at P-band over the two-month period. For the cross-polarized channel at P-band, the coherence remains high ($>$0.9) only for the first month, which is still long enough for a 21-day tomographic acquisition by BIOMASS. Temporal co-

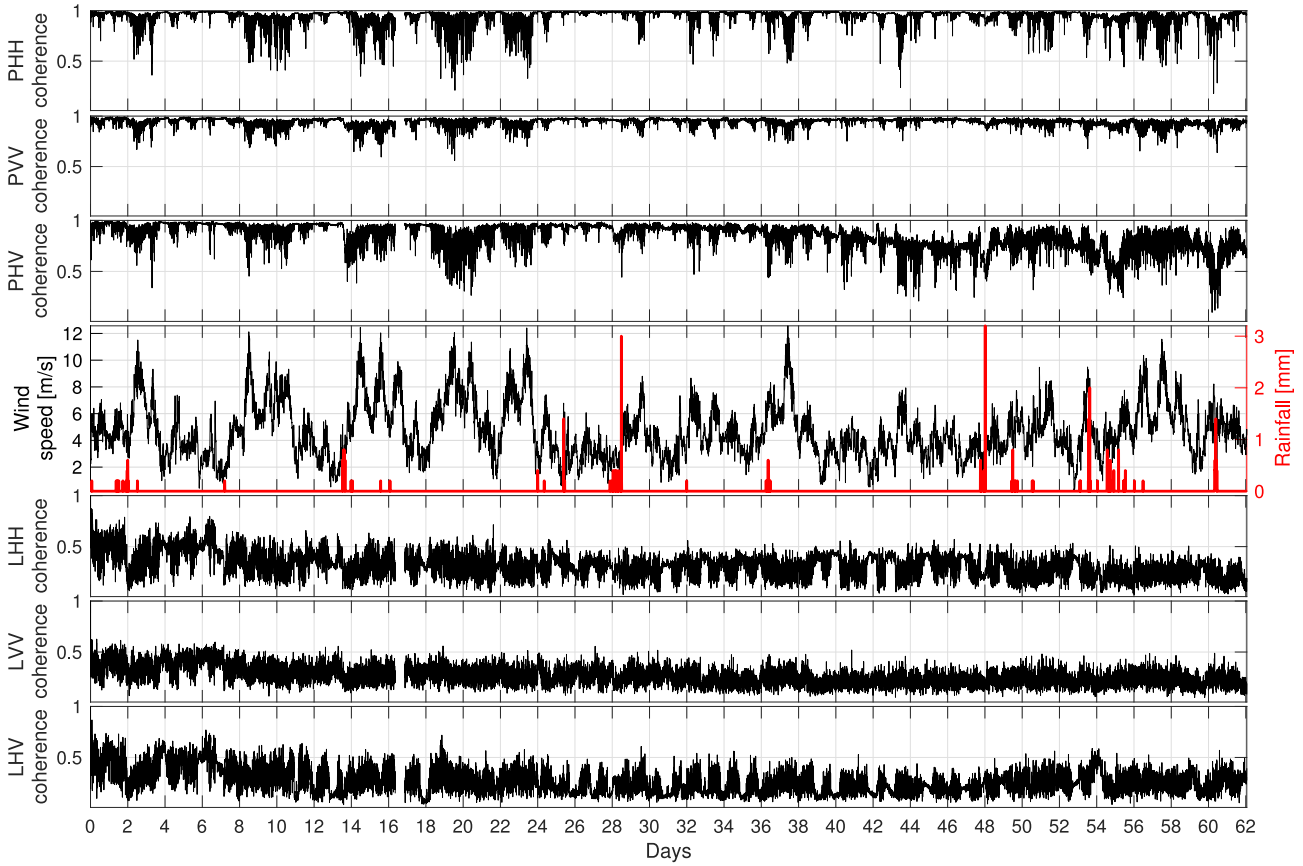

Fig. 15. Temporal coherence for P- and L-bands over a two-month period, starting at a time (June 10, 2017, 03:05) with a very low wind speed (∼0.5 m/s). High coherence is seen for P-band during quiet times for at least a month, whereas the L-band coherence degrades severely after a few hours after the reference time. Wind speeds above 5 m/s and rainfall severely degrades the temporal coherence for HH and HV at P-band, while VV coherence is more robust to environmental changes.

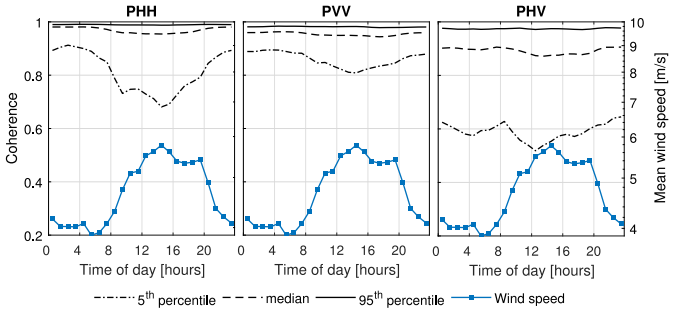

Fig. 16. Temporal coherence at different times of the day for P-band during the two-month summer period (Data set 2) is shown using the 5th, 50th (median), and 95th percentiles due to the skewed distributions. The blue curves with square markers indicate the average wind speed at different times of the day. Coherence is highest during night and early morning times when wind speeds are low.

herence at L-band is low (<0.8) after the first few hours following the reference time, especially during rain events and strong winds.

Temporal coherence at P-band during this two-month period is highest during the 22:00 to 07:00 h period, when the wind speed is low on average, as is shown in Fig. 16. This diurnal variation in temporal coherence at P-band is believed to be mostly due to wind speeds that exhibit a diurnal variation. Temporal coherence for HV is lower than the copolarized channels during all hours of the day, which is partly due to the decreased coherence in the second month when seasonal changes start to take place. These results indicate that evening to morning hours are most suitable for repeat-pass interferometric and tomographic SAR acquisitions at P-band. Such acquisitions at L-band over boreal forests taken during timescales of days or more will be severely degraded due to large temporal decorrelation.

VII. Summary and Conclusion

Radar signatures over a boreal forest stand were collected at 5 min intervals for HH, VV, and HV polarization at P- and L-bands from January to August 2017. Variations in the backscatter and temporal coherence were investigated.

During the winter, especially during subzero temperatures, the backscatter was seen to vary closely with temperature, causing changes of 4 to 10 dB. The backscatter stabilized after the winter. The HH- and VV-polarized backscatter showed a strong linear relationship at both P- and L-bands during subzero conditions. The HH/VV ratio was further shown to reduce the spread in backscatter measurements at P- and L-bands compared to HH and VV alone, motivating the ratio's use in biomass estimation models since it is sensitive to above-ground biomass. It was suggested that strong winds cause biases in P-band backscatter due to trees bending over a flat ground. Winds exhibited a diurnal

cycle during dry conditions, which caused a corresponding diurnal variation in the P-band backscatter. The P-band temporal coherence remained high for at least a month, except during windy conditions. These results discourage the use of repeat-pass interferometry and tomography acquisitions at P-band during windy conditions in boreal forests. But P-band coherence was highest during night and early morning times (22:00 to 7:00 h) when wind speeds were low on average. For biomass estimation models using only P-band backscatter, the HH/VV backscatter ratio showed some improved resilience to environmental variations during the summer compared to HH alone, but not VV. At L-band, winds caused a bias in the HV backscatter only, and the temporal coherence was poor for all channels over timescales of hours or more, strongly discouraging the use of repeat-pass interferometry and tomography at L-band, at least during the summer.

The BorealScat experiment will continue to collect data following the end of the period investigated in this study. The continued time series might explain some of the unexplained variations shown in this paper, such as the cause of variations in backscatter occurring over several weeks and erratic variations occurring on the time scale of days. Longer time series may also allow the separation of the effects on backscatter arising from different environmental parameters, allowing this dynamic process to be modeled. Improved calibration methods will allow the combination of antenna pairs to increase the number of looks, giving more reliable backscatter estimates during quiet conditions. Backscatter variations and temporal coherence will also be investigated from tomographic profiles, revealing changes at different heights. To support companion and tandem SAR missions, short-term decorrelation, especially at L-band, should be studied in more detail. Previous studies give reason to believe that moisture variations in the soil and tree trunks have a larger role to play in variations of the scattered field with time, which was not well covered in this study. Better information, in the form of new moisture sensor data and knowledge about tree physiology will give more insight into these mechanisms. Since August 17, 2017, the same fully polarimetric tomographic radar measurements are being made at C-band, enabling the same investigations in support of ESA's Sentinel-1 mission. Possible future companion satellites to the Sentinel-1 satellites will allow frequent single-pass interferometric SAR observations over boreal forests, for which temporal variations of coherence due to environmental parameters are of high importance [44].

ACKNOWLEDGMENT

The authors would like to thank Dr. M. Soja, Dr. L. Eriksson, and E. Blomberg at Chalmers University of Technology, Sweden, for their contributions to the BorealScat project. The MATLAB wavelet coherence toolbox was provided by A. Grinsted from Niels Bohr Institute, University of Copenhagen, Copenhagen, Denmark. Ground measurements resulting in biomass estimates were carried out by the Department of Forest Resource Management, Swedish University of Agricultural Sciences, Umeå, Sweden.

REFERENCES

[1] UN-REDD Programme. (2008). UN collaborative programme on reducing emissions from deforestation and forest degradation in developing countries (UN-REDD). UNEP Framework Document, FAO, UNDP, UNEP.

[2] R. Houghton, F. Hall, and S. Goetz, "Importance of biomass in the global carbon cycle," *J. Geophys. Res.: Biogeosci.*, vol. 114, no. 3, pp. 1–13, 2009.

[3] ESA, "Report for mission selection: BIOMASS," Tech. Rep. ESA SP-1324/1 (3 volume series), European Space Agency, Noordwijk, The Netherlands, 2012.

[4] WMO, "Implementation plan for the global observing system for climate in support of the UNFCCC," WMO/TD- No. 1219; GCOS- No. 92, World Meteorological Organization, Global Climate Observing System, Geneva, Switzerland, 2004.

[5] Y. Kankaku, S. Suzuki, and Y. Osawa, "ALOS-2 mission and development status," in *Proc. IEEE Int. Geosci. Remote Sens. Symp.*, 2013, pp. 2396–2399.

[6] A. Moreira *et al.*, "Tandem-L: A highly innovative bistatic SAR mission for global observation of dynamic processes on the Earth's surface," *IEEE Geosci. Remote Sens. Mag.*, vol. 3, no. 2, pp. 8–23, Jun. 2015.

[7] G. Sandberg, L. Ulander, J. Fransson, J. Holmgren, and T. Le Toan, "L- and P-band backscatter intensity for biomass retrieval in hemiboreal forest," *Remote Sens. Environ.*, vol. 115, no. 11, pp. 2874–2886, 2011.

[8] M. J. Soja, G. Sandberg, and L. M. Ulander, "Regression-based retrieval of boreal forest biomass in sloping terrain using P-band SAR backscatter intensity data," *IEEE Trans. Geosci. Remote Sens.*, vol. 51, no. 5, pp. 2646–2665, May 2013.

[9] G. Sandberg, L. Ulander, J. Wallerman, and J. Fransson, "Measurements of forest biomass change using P-band synthetic aperture radar backscatter," *IEEE Trans. Geosci. Remote Sens.*, vol. 52, no. 10, pp. 6047–6061, Oct. 2014.

[10] S. Saatchi, K. Halligan, D. Despain, and R. Crabtree, "Estimation of forest fuel load from radar remote sensing," *IEEE Trans. Geosci. Remote Sens.*, vol. 45, no. 6, pp. 1726–1740, Jun. 2007.

[11] M. Santoro, L. E. Eriksson, and J. E. Fransson, "Reviewing ALOS PALSAR backscatter observations for stem volume retrieval in Swedish forest," *Remote Sens.*, vol. 7, no. 4, pp. 4290–4317, 2015.

[12] B. Hallberg, G. Smith-Jonforsen, L. M. H. Ulander, and G. Sandberg, "A physical-optics model for double-bounce scattering from tree stems standing on an undulating ground surface," *IEEE Trans. Geosci. Remote Sens.*, vol. 46, no. 9, pp. 2607–2621, Sep. 2008.

[13] C. Albinet, P. Borderies, N. Floury, and E. Pottier, "Measure of temporal variation of P-Band radar cross section and temporal coherence of a temperate tree," *IEEE Trans. Geosci. Remote Sens.*, vol. 54, no. 11, pp. 6255–6264, Nov. 2016.

[14] J. Van Zyl, "The effect of topography on radar scattering from vegetated areas," *IEEE Trans. Geosci. Remote Sens.*, vol. 31, no. 1, pp. 153–160, Jan. 1993.

[15] G. Smith and L. M. H. Ulander, "A model relating VHF-band backscatter to stem volume of coniferous boreal forest," *IEEE Trans. Geosci. Remote Sens.*, vol. 38, no. 2, pp. 728–740, Mar. 2000.

[16] J. Fransson, G. Smith, F. Walter, A. Gustavsson, and L. Ulander, "Estimation of forest stem volume in sloping terrain using CARABAS-II VHF SAR data," *Can. J. Remote Sens.*, vol. 30, no. 4, pp. 651–660, 2004.

[17] G. Smith-Jonforsen, L. M. H. Ulander, and X. Luo, "Low VHF-band backscatter from coniferous forests on sloping terrain," *IEEE Trans. Geosci. Remote Sens.*, vol. 43, no. 10, pp. 2246–2260, Oct. 2005.

[18] D. P. Belcher and N. C. Rogers, "Theory and simulation of ionospheric effects on synthetic aperture radar," *IET Radar, Sonar Navig.*, vol. 3, no. 5, pp. 541–551, 2009.

[19] H. Zebker and J. Villasenor, "Decorrelation in interferometric radar echoes," *IEEE Trans. Geosci. Remote Sens.*, vol. 30, no. 5, pp. 950–959, Sep. 1992.

[20] S.-K. Lee, F. Kugler, K. Papathanassiou, and I. Hajnsek, "Quantification of temporal decorrelation effects at L-band for polarimetric SAR interferometry applications," *IEEE J. Sel. Topics Appl. Earth Observ. Remote Sens.*, vol. 6, no. 3, pp. 1351–1367, Jun. 2013.

[21] C. Albinet *et al.*, "TropiSCAT: A ground based polarimetric scatterometer experiment in tropical forests," *IEEE J. Sel. Topics Appl. Earth Observ. Remote Sens.*, vol. 5, no. 3, pp. 1060–1066, Jun. 2012.

[22] C. Albinet *et al.*, "First results of AfriScat, a tower-based radar experiment in African forest," in *Proc. IEEE Int. Geosci. Remote Sens. Symp.*, 2015, pp. 5356–5358.

[23] H. Keith, B. Mackey, and D. Lindenmayer, "Re-evaluation of forest biomass carbon stocks and lessons from the world's most carbon-dense forests," *Proc. Nat. Acad. Sci. USA*, vol. 106, no. 28, pp. 11635–11640, 2009.
[24] P. Hari and L. Kulmala, *Boreal Forest and Climate Change*. New York, NY, USA: Springer, 2008.
[25] L. M. H. Ulander, M. J. Soja, A. R. Monteith, L. E. B. Eriksson, and J. E. S. Fransson, "BorealScat: A tower experiment for understanding temporal changes in P- and L-band backscattering from a boreal forest," in *Proc. Living Planet Symp.*, Prague, Czech Republic, May 9–13, 2016.
[26] A. R. Monteith, M. J. Soja, L. M. H. Ulander, and L. E. B. Eriksson, "BorealScat: A tower-based tomographic and polarimetric radar experiment in the boreal forest at P-, L- and C-band," in *Proc. IEEE Int. Geosci. Remote Sens. Symp.*, Jul. 2016, pp. 7458–7461.
[27] G. Torgovnikov, *Dielectric Properties of Wood and Wood-Based Materials*. New York, NY, USA: Springer, 2012.
[28] K. C. McDonald, R. Zimmermann, and J. S. Kimball, "Diurnal and spatial variation of xylem dielectric constant in Norway spruce (Picea abies [L.] Karst.) as related to microclimate, xylem sap flow, and xylem chemistry," *IEEE Trans. Geosci. Remote Sens.*, vol. 40, no. 9, pp. 2063–2082, Sep. 2002.
[29] J. Wolfe and G. Bryant, "Cellular cryobiology: Thermodynamic and mechanical effects," *Int. J. Refrigeration*, vol. 24, no. 5, pp. 438–450, 2001.
[30] G. Neuner, B. Xu, and J. Hacker, "Velocity and pattern of ice propagation and deep supercooling in woody stems of Castanea sativa, Morus nigra and Quercus robur measured by IDTA," *Tree Physiology*, vol. 30, no. 8, pp. 1037–1045, 2010.
[31] G. Charrier *et al.*, "Monitoring of freezing dynamics in trees: A simple phase shift causes complexity," *Plant Physiology*, vol. 173, no. 4, pp. 2196–2207, 2017.
[32] V. Artemov and A. Volkov, "Water and ice dielectric spectra scaling at 0° C," *Ferroelectrics*, vol. 466, no. 1, pp. 158–165, 2014.
[33] J. Way *et al.*, "The effect of changing environmental conditions on microwave signatures of forest ecosystems: Preliminary results of the March 1988 Alaskan aircraft SAR experiment," *Int. J. Remote Sens.*, vol. 11, no. 7, pp. 1119–1144, 1990.
[34] N. Ackermann, *Growing Stock Volume Estimation in Temperate Forested Areas Using a Fusion Approach With SAR Satellites Imagery*. New York, NY, USA: Springer, 2015.
[35] J. Pulliainen, L. Kurvonen, and M. Hallikainen, "Multitemporal behavior of L- and C-band SAR observations of boreal forests," *IEEE Trans. Geosci. Remote Sens.*, vol. 37, no. 2, pp. 927–937, Mar. 1999.
[36] E. Rignot, J. Way, and L. Viereck, "Radar estimates of aboveground biomass in boreal forests of interior Alaska," *IEEE Trans. Geosci. Remote Sens.*, vol. 32, no. 5, pp. 1117–1124, Sep. 1994.
[37] M. Santoro, J. Fransson, L. Eriksson, M. Magnusson, L. Ulander, and H. Olsson, "Signatures of ALOS PALSAR L-band backscatter in Swedish Forest," *IEEE Trans. Geosci. Remote Sens.*, vol. 47, no. 12, pp. 4001–4019, Dec. 2009.
[38] H. Petersson, "Biomassafunktioner för trädfaktorer av tall, gran och björk i Sverige *(Swedish)* (Eng: *Biomass Functions for Tree Parameters of Pine, Spruce and Birch in Sweden)*," Tech. Rep., Swedish Univ. Agricultural Sci., Umeå, Sweden, 1999.
[39] M. H. Trauth, R. Gebbers, N. Marwan, and E. Sillmann, *MATLAB Recipes for Earth Sciences*, vol. 34. New York, NY, USA: Springer, 2007.
[40] A. Grinsted, J. C. Moore, and S. Jevrejeva, "Application of the cross wavelet transform and wavelet coherence to geophysical time series," *Nonlinear Processes Geophysics*, vol. 11, nos. 5/6, pp. 561–566, 2004.
[41] C. Torrence and G. P. Compo, "A practical guide to wavelet analysis," *Bull. Am. Meteorological Soc.*, vol. 79, no. 1, pp. 61–78, 1998.
[42] J. P. Sparks, G. S. Campbell, and A. R. Black, "Water content, hydraulic conductivity, and ice formation in winter stems of Pinus contorta: A TDR case study," *Oecologia*, vol. 127, no. 4, pp. 468–475, 2001.
[43] D. M. Gates, "Water relations of forest trees," *IEEE Trans. Geosci. Remote Sens.*, vol. 29, no. 6, pp. 836–842, Nov. 1991.
[44] H. Rott *et al.*, "SESAME: A single-pass interferometric Sentinel-1 companion SAR mission for monitoring geo- and biosphere dynamics," in *Proc. IEEE Int. Geosci. Remote Sens. Symp.*, Jul. 23–28, 2017, pp. 107–110.

Albert R. Monteith (S'09) received the M.Sc. degree in electrical engineering from Chalmers University of Technology, Gothenburg, Sweden, in 2015, where he is currently working toward the Ph.D. degree in radar remote sensing of boreal forests with the Department of Space, Earth and Environment.

His main research interests include microwave remote sensing with applications in forestry.

Lars M. H. Ulander (S'86–M'90–SM'04–F'17) received the M.Sc. degree in engineering physics and the Ph.D. degree in electrical and computer engineering from Chalmers University of Technology, Gothenburg, Sweden, in 1985 and 1991, respectively.

Since 1995, he has been with the Swedish Defence Research Agency (FOI), Kista, Stockholm, where he is the Director of research in radar signal processing and leads the research on very high-frequency/ultrahigh-frequency band radar. Since 2014, he has been a Professor in radar remote sensing with Chalmers University of Technology. He is the author or coauthor of more than 300 professional publications, of which more than 60 are in peer-reviewed scientific journals. He is the holder of five patents. His research interests include synthetic aperture radar, electromagnetic scattering models, and remote sensing applications.